

An X-ray spectroscopy study of structural stability of superhydrogenated pyrene derivatives

Yining Huo,¹ Mónica K. Espinoza Cangahuala,¹ Vicente Zamudio-Bayer^{1b},² Marcelo Goulart,¹ Markus Kubin,² Martin Timm,² J. Tobias Lau,^{2,3} Bernd von Issendorff,³ Ronnie Hoekstra,^{1,4} Shirin Faraji^{1★} and Thomas Schlathölter^{1b,5★}

¹Zernike Institute for Advanced Materials, University of Groningen, Nijenborgh 4, NL-9747AG Groningen, the Netherlands

²Abteilung für Hochempfindliche Röntgenspektroskopie, Helmholtz-Zentrum Berlin für Materialien und Energie, Berlin D-12489, Germany

³Physikalisches Institut, Universität Freiburg, D-79104 Freiburg, Germany

⁴Advanced Research Center for Nanolithography (ARCNL), Science Park 106, NL-1098 XG Amsterdam, the Netherlands

⁵University College Groningen, University of Groningen, Hoendiepskade 23/24, NL-9718 BG Groningen, the Netherlands

Accepted 2023 April 26. Received 2023 April 25; in original form 2023 February 15

ABSTRACT

The stability of polycyclic aromatic hydrocarbons (PAHs) upon soft X-ray absorption is of crucial relevance for PAH survival in X-ray dominated regions. PAH stability depends on molecular size but also on the degree of hydrogenation that is related to H₂ formation in the interstellar medium. In this project, we intend to reveal the changes of electronic structure caused by hydrogenation and the impact of hydrogenation on the stability of the carbon backbone for cationic pyrene and its hydrogenated derivatives by analysis of near C K-edge soft X-ray photoions. In our experiments, the PAH cations were trapped in a cryogenic radiofrequency linear ion trap and exposed to monochromatic X-rays with energies from 279 to 300 eV. The photoproducts were mass-analysed by means of time-of-flight spectroscopy. Partial ion yields were then studied as a function of photon energy. X-ray absorption spectra computed by time-dependent density functional theory (TD-DFT) aided the interpretation of the experimental results. A very good agreement between experimental data and TD-DFT with short-range corrected functionals for all PAH ions was reached. The near-edge X-ray absorption mass spectra exhibit clear peaks due to C 1s transitions to singly occupied molecular orbitals and to low-lying unoccupied molecular orbitals. In contrast to coronene cations, where hydrogen attachment drastically increases photostability of coronene, the influence of hydrogenation on photostability is substantially weaker for pyrene cations. Here, hydrogen attachment even destabilizes the molecular structure. An astrophysical model describes the half-life of PAH ions in interstellar environments.

Key words: astrochemistry – molecular data – molecular processes – ISM: molecules.

1 INTRODUCTION

Polycyclic Aromatic Hydrocarbons (PAHs) consisting of multiple aromatic rings of carbon atoms are believed to exist in a variety of astronomical environments, both in ionic and neutral form. PAHs are the most likely carriers of the aromatic infrared (IR) bands in the interstellar medium (ISM) (Tielens 2008; Peeters et al. 2021; Zettergren et al. 2021). In the ISM PAHs can be electronically excited by means of ultraviolet or vacuum ultraviolet (VUV) photoexcitation. The electronic excitation is then internally converted into vibrational modes that de-excite mostly by IR emission.

X-ray induced photofragmentation processes dominate in molecular clouds surrounding X-ray sources, commonly referred to as X-ray dominated regions (XDRs). Examples are planetary nebulae (PNe) (Kastner, Vrtilik & Soker 2001; Zhang, Kwok & Dinh-V-Trung 2008; Montez & Kastner 2018), supernova remnants (Vink 2012;

Oskinova et al. 2020), and active galactic nuclei (AGN) (Jiménez-Bailón et al. 2005; Aalto et al. 2012; Costagliola et al. 2016; Puccetti et al. 2016; Hickox & Alexander 2018; Salak et al. 2018), and young stellar objects (Rab et al. 2018; Gavilan et al. 2022). For instance, NGC 7027 is a very high temperature PN, that exhibits bright soft X-ray emission as observed by the *Chandra X-Ray Observatory* for the broad 0.2–3 keV band (Kastner et al. 2001). Based on data from the *Stratospheric Observatory for Infrared Astronomy (SOFIA) telescope*, Lau et al. investigated the spatial distribution of the 6.2 μm PAH emission feature in this PN (Lau et al. 2016). They report evidence of efficient PAH formation which entails the question whether or not PAHs are sufficiently stable to survive and possibly grow under these harsh conditions.

It is well established that PAH photostability increases with PAH size (Zhen et al. 2015, 2016), but also hydrogen attachment can have a substantial influence. Cazaux and coworkers have shown that exposure of gas-phase coronene cations to atomic hydrogen leads to successive hydrogen attachment via a well-defined sequence involving alternating reaction barriers and vastly different binding

* E-mail: s.s.faraji@rug.nl (SF); t.a.schlatholter@rug.nl (TS)

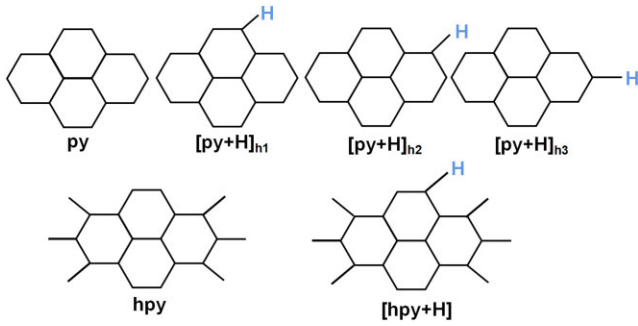


Figure 1. Top row, from left to right: The structures of py, [py + H]_{h1}, [py + H]_{h2}, and [py + H]_{h3}. The indices h1, h2, and h3 indicate three different outer edge hydrogen attachment sites for [py+H]. Bottom row, from left to right: The structure of hpy and [hpy + H]. Only four hpy outer edge sites can accommodate hydrogen attachment which are symmetrically equivalent.

energies (Boschman et al. 2012; Cazaux et al. 2016, 2019). The precise effect of hydrogenation on PAH stability has been debated over the last years. Soft X-ray photoabsorption experiments have shown that attachment of several H atoms to coronene cations ($C_{24}H_{12}^+$) can protect the coronene backbone from fragmentation (Reitsma et al. 2014). In collision experiments it was subsequently shown that the molecular skeleton of hexahydro-pyrene ($C_{16}H_{16}$) and dodecahydro-pyrene ($C_{16}H_{22}$) is actually weakened as compared to regular pyrene ($C_{16}H_{10}$) (Gatchell et al. 2015). In these pyrene studies PAH hydrogenation was more extensive as compared to the coronene experiment. Cazaux et al. employed IR spectroscopy to show that for coronene cations, a transition from protection to weakening occurs for attachment of more than 9 H atoms (Cazaux et al. 2019). A similar observation was made by Stockett et al. in a systematic VU photofragmentation study that demonstrated a protective effect for neutral pyrene up to attachment of 4 H atoms, whereas addition of 6 hydrogen atoms proved to be de-stabilizing (Stockett et al. 2021). A number of open questions remain. It is for instance unclear in how far the PAH charge state influences stability (coronene has been studied in cationic form whereas neutral pyrene was investigated) or what the influence of a radical/non-radical electron configuration is.

A straightforward way to tackle these open questions is a systematic photofragmentation study on cationic pyrene derivatives in the soft X-ray regime, which allows for a direct comparison to previous studies on cationic coronene. The soft X-ray range of photon energies is interesting by itself for two reasons. XDRs and thus soft X-ray induced fragmentation of molecules are ubiquitous in some astrophysical environments and in particular in PNe. A number of laboratory experiments focusing on X-ray interactions with carbonaceous molecular ions were reported recently (Reitsma et al. 2014, 2015; Qutián-Lara et al. 2018; Qutián-Lara et al. 2020; Huo et al. 2022).

In the following, we address PAH backbone fragmentation as well as H loss from intact PAH dications and trications as a function of soft X-ray photon energy. The prototype PAH molecules we use are pyrene (py, $C_{16}H_{10}$) and its superhydrogenated derivative hexahydro-pyrene (hpy, $C_{16}H_{16}$) in their cationic state (py^+ and hpy^+ , respectively). In addition, their singly-hydrogenated counterparts $[py + H]^+$ ($C_{16}H_{11}^+$), and $[hpy + H]^+$ ($C_{16}H_{17}^+$) are studied to assess the effect of the addition of a single H atom on the stability of py^+ and hpy^+ . The molecular structures of py and hpy and their singly hydrogenated counterparts are depicted in Fig. 1. From previous studies it is known that for the first hydrogen attachment, edge positions are energetically favoured (Cazaux et al. 2016). Because

of the D_{2h} symmetry of py, three different [py + H] isomers can be formed which are labelled by h1, h2, and h3 subscripts. It is of note that the H attachment breaks the D_{2h} symmetry. For hpy, the four outer edge sites available for hydrogen attachment are symmetrically equivalent.

Throughout the paper for ease of identification of the four different parent cations, the following colour code will be used py^+ - black, $[py + H]^+$ - red, hpy^+ - blue, and $[hpy + H]^+$ - cyan, unless stated otherwise.

2 EXPERIMENT

The experimental data presented in this work were obtained using the Ion Trap end-station (Hirsch et al. 2009; Niemeyer et al. 2012; Langenberg et al. 2014) at the UE52-PGM high-resolution soft X-ray beamline at the BESSY II synchrotron facility at the Helmholtz Zentrum Berlin. High-purity samples of py and hpy molecules were purchased from Sigma Aldrich. A saturated solution of the PAH molecules in methanol was prepared. This solution was then diluted by adding methanol with 1:1 ratio in volume. A 5 ml diluted PAH solution was mixed with 0.5 ml $AgNO_3$ (10 mmol L^{-1}) for facilitating PAH cation formation, by means of the chemical reaction: $C_{16}H_{10} + Ag^+ \rightarrow Ag + C_{16}H_{10}^+$.

We employed electrospray ionization to bring the analyte cations into the gas phase. A radiofrequency (RF) ion funnel was used to compress the phase-space of the electrosprayed PAH cation beam. The ions were then transported through a RF hexapole ion guide, where the ions could be exposed to a beam of atomic hydrogen, produced in a 27 MHz discharge source (Hoekstra et al. 1989). To avoid propagation of UV photons from the plasma into the hexapole chamber, an optically blind teflon capillary system (Blick et al. 1998) was employed. This system is known to reach a dissociation degree of ≈ 30 per cent (Boschman et al. 2012). Atomic hydrogen attachment could only occur during the passage of PAH cations through the hexapole, i.e. within a short time window. Therefore almost solely single hydrogen attachment was observed in subsequent mass-selection by an RF quadrupole mass filter. The mass-selected PAH cations were deflected under 90° by an electrostatic quadrupole deflector and injected into a cryogenic ($T \approx 20 \text{ K}$) linear RF ion trap.

In the linear RF trap, the PAH cations were exposed to a collinear beam of monochromatic soft X-rays ($\Delta E \approx 50 \text{ meV}$) with fluxes in the $10^{12} \text{ photon s}^{-1}$ range. Cationic photoproducts were extracted into a reflectron-type time of flight (TOF) mass spectrometer and detected by a micro channel plate detector. We performed near-edge X-ray absorption mass spectra (NEXAMS) experiments, i.e. the soft X-ray energy $E_{X\text{-ray}}$ was ramped in small steps across the C K-edge (279–300 eV). For each and every photon energy $E_{X\text{-ray}}$, photofragmentation TOF spectra were recorded.

3 THEORY

The theoretical approach has been described in detail in our previous work on coronene cations (Huo et al. 2022). In short, time-dependent density functional theory (TD-DFT) in the adiabatic approximation (Besley, Peach & Tozer 2009) was used to compute X-ray absorption spectra. The ground-state geometries of the gas-phase py^+ and $[py + H]^+$ were optimized at the $\omega B97XD/cc\text{-pVDZ}$ theory level. A vibrational frequency analysis at the same theory level was performed to check for imaginary frequencies and confirm convergence of the optimized molecular structures. Subsequently, C 1s excitations were

computed by means of TD-DFT within the Tamm-Dancoff approximation (Hirata & Head-Gordon 1999). Here, we used the SRC-2-R1-D2 functional developed by Besley and coworkers (Besley et al. 2009; Besley & Asmuruf 2010) as implemented in the Q-CHEM 5.2.2 quantum chemistry package (Epifanovsky et al. 2021). In the SRC functional, the exchange functional is described by the Becke functional (Becke 1988) and the correlation functional is based on a combination of the Lee-Yang-Parr (LYP) functional (Lee, Yang & Parr 1988) and the Vosko-Wilk-Nusair functional (Vosko, Wilk & Nusair 1980). 1000 carbon core excited-state transitions were calculated for the py^+ radical cation and for various $[\text{py} + \text{H}]^+$ cation isomers, respectively. More details about transition are presented in supplementary material.

Adiabatic dissociation energies (ADEs) for loss of neutral and ionic H, H_2 were computed as the difference in energy between reactants and products. Because of the large amount of deposited energy in X-ray photon absorption processes, transition states and barriers were not investigated. All ADE calculations including optimization and frequency analysis were performed at the B3LYP/6-31G(d) level, as implemented in the ORCA program package (Lehtola et al. 2018). The scaling factor 0.9806 was adopted to correct the zero-point energy (Scott & Radom 1996).

4 RESULTS AND DISCUSSION

4.1 Mass spectra

In this study, soft X-ray photofragmentation of py^+ , $[\text{py} + \text{H}]^+$, hpy^+ , and $[\text{hpy} + \text{H}]^+$ was investigated over the photon energy range from 279 to 300 eV, which encompasses the C K-edge. Most extensive fragmentation is observed for the highest photon energies at which direct 1s photoionization is possible. Subsequent Auger decay to the photoinduced 1s vacancy leads to emission of one (or more) additional electrons. Therefore almost all fragmentation processes start from an (at least) triply charged ion.

Mass spectra of 300 eV soft X-ray induced photoproducts for all four molecular ions under study are presented in Fig. 2. For all four systems, qualitatively similar fragmentation patterns are observed: The highest peaks are always observed in the M/q range between 48 and 78 (M and q stand for the mass and charge state of the molecule, respectively). Peak assignment is not always straightforward, as photoproducts can come in different masses and charge states which may coincide in M/q . Postma et al. have illustrated this for keV ion induced fragmentation of anthracene (Postma et al. 2010). Most peaks occur in C_mH_n^q groups with a fixed number of carbon atoms m and a variable number of hydrogen atoms n . Monocationic fragments ($q = 1$) are most intense, with carbon numbers m ranging from 2 to 8.

For every given m , a number of peaks due to different numbers of hydrogen atoms n can be observed at integer M/q values. In many cases, additional peaks at half-integer M/q can be observed, which can only be due to dicationic fragments ($q = 2$). A good example is the C_5H_n^+ group that for all four molecules clearly contains a weaker contribution of $\text{C}_{10}\text{H}_n^{2+}$. The precise ratio of monocationic and dicationic contribution to a group of peaks is difficult to quantify, as integer peaks coincide. Dicationic fragments with an odd number of carbon atoms can be observed as well, e.g. $\text{C}_9\text{H}_n^{2+}$ between C_4H_n^+ and C_5H_n^+ . Such fragment groups are solely due to dications and can thus help to estimate the total contribution of dicationic fragments to the spectrum. Dications can be clearly identified for the range from $m = 7$ to $m = 11$ for py^+ and to $m = 15$ for hpy^+ . Fragments with $m \leq 8$ typically accommodate a single positive charge, only.

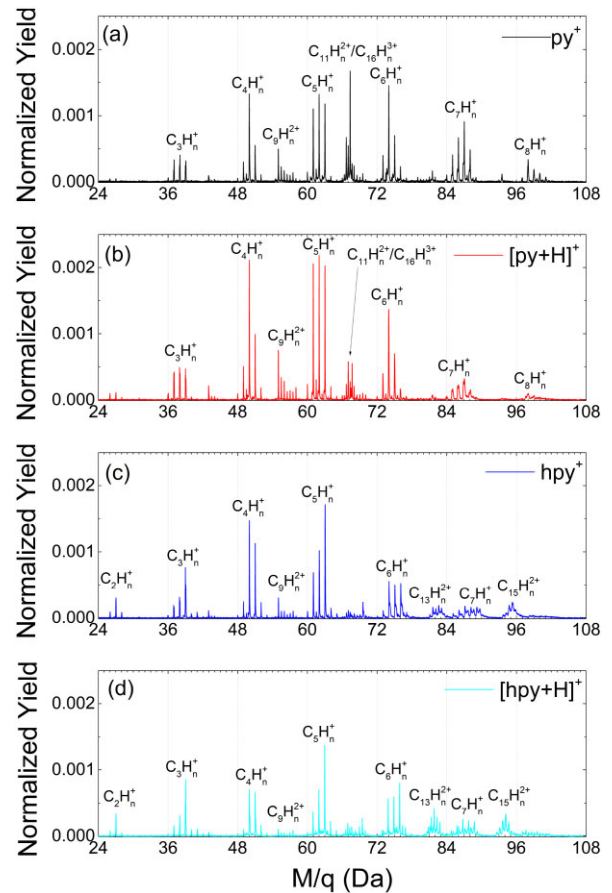


Figure 2. Mass spectra of py^+ , $[\text{py} + \text{H}]^+$, hpy^+ , and $[\text{hpy} + \text{H}]^+$ induced by 300 eV. All spectra are normalized to the respective total ionic fragments yields. Predominate clusters of fragments have been labelled.

Tricationic fragments $\text{C}_{16}\text{H}_n^{3+}$ with an intact carbon backbone are observed for all four molecules, though only very weakly for hpy^+ and $[\text{hpy} + \text{H}]^+$. It is to be noted that the corresponding $\text{C}_{16}\text{H}_n^{2+}$ dications are only observed at photon energies below the 1s ionization threshold. Large dicationic fragments that underwent loss into $\text{C}_{13}\text{H}_n^{2+}$ and $\text{C}_{15}\text{H}_n^{2+}$ are only observed for hpy^+ and $[\text{hpy} + \text{H}]^+$.

Single hydrogenation of py^+ into $[\text{py} + \text{H}]^+$ leads to a relative increase of C_3H_n^+ , C_4H_n^+ , and C_5H_n^+ . $\text{C}_{16}\text{H}_n^{3+}$ yields on the other hand are suppressed by hydrogenation.

Attachment of a single H atom to hpy^+ leads to overall reduced C_mH_n^+ yields for $m = 3$ to $m = 6$. This is in stark contrast to our previous observations for coronene cations (Huo et al. 2022), where the opposite was observed. The relatively large dicationic fragments $\text{C}_{13}\text{H}_n^{2+}$ and $\text{C}_{15}\text{H}_n^{2+}$ only appear for the strongly hydrogenated hpy^+ and $[\text{hpy} + \text{H}]^+$ precursors, indicating the ability of these systems to accommodate more charge.

Naturally, for hpy^+ and $[\text{hpy} + \text{H}]^+$, the various C_mH_n^q groups exhibit higher average hydrogen content than what is observed for py^+ and $[\text{py} + \text{H}]^+$. This finding reflects simply the larger number of H atoms present in the precursor ion.

For photon energies below the carbon 1s binding energy, 1s excitation rather than ionization is induced. As a consequence, the monocationic precursor is not further ionized in the photoabsorption process. Subsequent Auger decay of the photoinduced 1s vacancy will lead to emission of one or more Auger electrons. Fragmentation will therefore typically start from a doubly charged molecular ion.

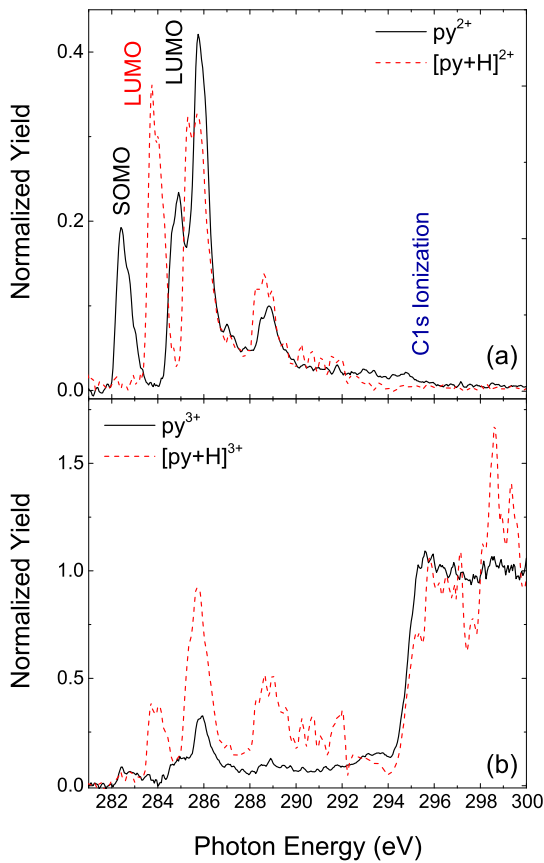


Figure 3. Top panel: NEXAMS data for $C_{16}H_{10}^{2+}$ from py^+ and $C_{16}H_{11}^{2+}$ from $[py + H]^+$ (normalized to the integral of the total yields in excitation range). Bottom panel: NEXAMS data for $C_{16}H_{10}^{3+}$ from py^+ and $C_{16}H_{11}^{3+}$ from $[py + H]^+$ (bottom panel, normalized to the ionization continuum). Transitions to singly occupied molecular orbital (SOMO) and lowest unoccupied molecular orbital (LUMO) are indicated. The $1s$ binding energy is around 295 eV where a threshold-like increase of trication yields is observed.

A more quantitative investigation of partial ion yields (PIYs) in the excitation and in the ionization regime can be found in part 1 of the supplementary information.

4.2 NEXAMS spectra

A deeper look into the influence of photon energy on molecular fragmentation is possible by investigation of selected fragment yields as a function of photon energy. Fig. 3 displays such NEXAMS spectra for non-dissociative single ionization (NDSI) and for non-dissociative double ionization (NDDI) of py^+ and $[py + H]^+$. The top spectrum shows the NDSI data, i.e. PIYs of $C_{16}H_{10}^{2+}$ formed from py^+ and for $C_{16}H_{11}^{2+}$ formed from $[py + H]^+$. As discussed before, NDSI is very unlikely in the $1s$ -ionization regime, where $1s$ ionization is usually followed by Auger relaxation releasing one more electron. Therefore, (almost) all intensity of the dication spectra is below the ionization threshold. The peaks are signatures of specific resonant $1s$ excitations to unoccupied molecular orbitals.

The py^+ cation is a radical cation i.e. it features a SOMO as its highest occupied molecular orbital. The $1s$ -SOMO transition occurs at about 282.5 eV. At about 285 eV, $1s$ excitation to the LUMO is observed. The strongest peak is found at 286 eV and a fourth maximum is observed at about 289 eV. In $[py + H]^+$, there is no SOMO and the lowest-energy peak is the $1s$ -LUMO transition at

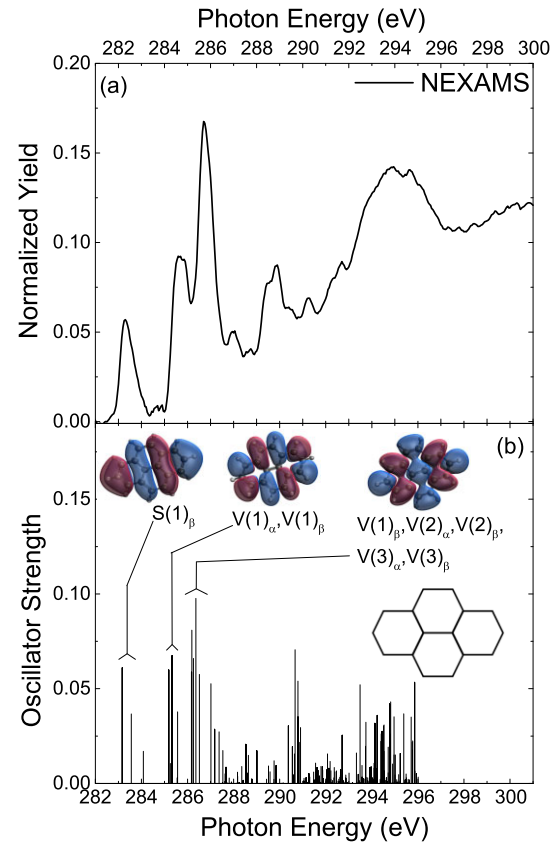


Figure 4. (a) $C_5H_5^+$ NEXAMS spectrum for py^+ . (b) TD-DFT stick spectrum of oscillator strengths for py^+ . Selected final states are shown as molecular orbitals. ‘S’ and ‘V’ indicate SOMO and unoccupied orbitals, respectively. Theoretical data has only been calculated up to 296 eV.

~284 eV. The two remaining peaks are only weakly affected by hydrogen attachment.

The bottom spectrum of Fig. 3 displays the data for NDDI, i.e. py^+ ionization into $C_{16}H_{10}^{3+}$. Below the ionization threshold, trication yields are low but feature the same peak positions as observed for NDSI. These low yields are expected as the Auger process that follows resonant $1s$ excitation here needs to be accompanied by the emission of two electrons, a process that has much smaller probability. Above the carbon $1s$ ionization energy, the PIY quickly increases until a plateau is reached.

For the hydrogenated $[py + H]^+$, the spectrum is different. In particular the ratio between NDDI below and above the ionization threshold differs significantly from the case of the py^+ cation. For $[py + H]^+$ the peaks in the excitation regime are relatively much more intense, with the 286 eV resonance reaching the same intensity as observed above the ionization threshold. As a consequence, the threshold like increase around the $1s$ ionization energy is much less pronounced for $[py + H]^+$.

For a more detailed interpretation of the experimental data, it is crucial to assign particular final molecular orbitals to the NEXAMS spectral features by means of TD-DFT calculations.

4.3 Theoretical spectra

The intensities (oscillator strengths) for carbon $1s$ excitation of py^+ and $[py + H]^+$ are shown in Figs 4–5 as stick spectra.

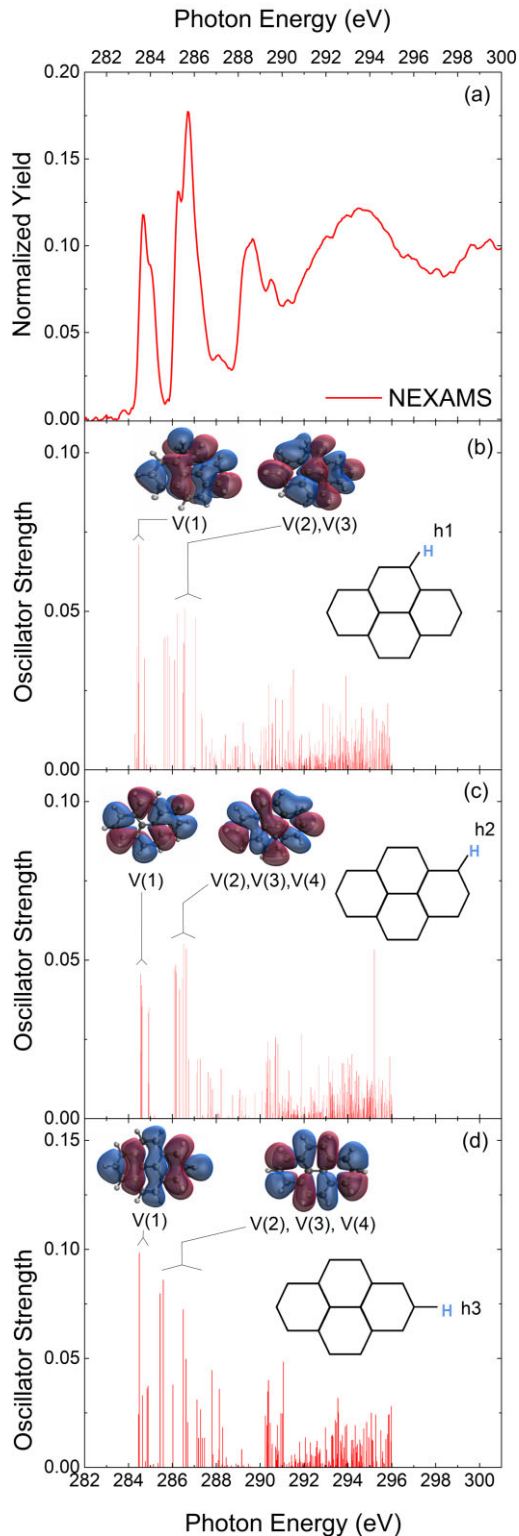


Figure 5. (a) $C_5H_3^+$ NEXAMS spectrum for $[py + H]^+$. (b, c, and d) TD-DFT calculated stick spectrum of oscillator strengths for the three different isomers of $[py + H]^+$ ($[py + H]_{h1}^+$, $[py + H]_{h2}^+$, and $[py + H]_{h3}^+$). Selected final states are shown as molecular orbitals. Theoretical data has only been calculated up to 296 eV.

For a first direct comparison between experimental data and theory, for all four precursor ions we have chosen the yield of the $C_5H_3^+$ fragment, as it is high for all precursors. It should be noted that in all four figures the photon energy axes of the experiment (top axes) and theory (bottom axes) are matched via shifting the energy axis of the simulated spectra by -1 eV.

The very small mismatch between the energy axes is a signature of the high quality of the calculations and the appropriateness of the functionals used.

Fig. 4 shows the results for py^+ precursor radical cations. Experiment and theory clearly are in very good agreement, allowing for an assignment of specific final molecular orbitals to the observed spectral features. As expected, the transitions that contribute to the lowest energy peak all have the SOMO $[S(1)_\beta]$ as final state. Different transition energies contributing to the SOMO peak stem from differences in binding energies of the $1s$ initial states associated with specific positions of the C atoms in the py^+ cation. The 16 C atoms can be roughly divided in the following three categories: two inner atoms, four inner-edge atoms, and 10 outer-edge atoms. The peak structures around 285 eV in the NEXAMS spectrum arise from $1s$ transitions to the lowest unoccupied orbitals which are labelled as $V(k)_\alpha$ or $V(k)_\beta$, with index k and with α and β indicating the two possible spin orientations. Isosurfaces of the electron density of the SOMO and the two energetically lowest unoccupied orbitals are added. The low-lying LUMO states have π^* character. Energetically higher transitions at 294 eV and above and the broad continuum are due to a multitude of higher excited states. With increasing transition energy, final states with a stronger σ^* character are reached.

Fig. 5 shows a similar comparison for hydrogenated pyrene cations $[py + H]^+$. For this precursor, three different hydrogenation sites are possible (see Fig. 1) and the corresponding isomers are referred to as h1, h2, and h3. The respective isosurface plots reveal the loss of symmetry induced by hydrogen attachment. A comparison of experimental and theoretical data shows that the gap experimentally observed between the two lowest transition energy peaks (Fig. 5a) is not present in the stick spectrum for isomer h3 (Fig. 5d). The other two isomers, h1 and h2, do agree well with the experimental data, suggesting that one or both of these isomers are dominating. It has to be noted, though that only two H attachment sites correspond to h3 whereas four sites whereas in total eight positions (four for h1 and four for h2) are available to h1 and h2.

When comparing py^+ (Fig. 4) and $[py + H]^+$ (Fig. 5), the most obvious difference is the absence of the SOMO peak for $[py + H]^+$. Furthermore, particularly the lowest-energy transitions are affected by the presence of the H atom. For py^+ , the first π^* -band involves the $V(1)_\alpha$ and $V(1)_\beta$ final orbitals whereas the second π^* -band is mainly involves $V(1)_\beta$, $V(2)_\alpha$, $V(2)_\beta$, $V(3)_\alpha$, and $V(3)_\beta$ final orbitals. For $[py + H]^+$, the first peak involves $V(1)$ final orbitals and the second peak includes $V(2)$, $V(3)$, and $V(4)$ final orbitals. The energy gap between the two lowest energy peaks approximately doubles from almost 1 to 2 eV. The widening appears to be primarily due to the shift of ~ 0.75 eV of the LUMO- $V(1)$ transitions to lower energies and now appears as a separated peak. Just like for py^+ , all final orbitals $V(1)$ to $V(4)$ have π^* -character and for higher energies transitions start to populate more and more states with σ^* character.

The theoretical data for hpy^+ and $[hpy + H]^+$ can be found in the supplementary information.

4.4 Fragmentation dynamics

In our previous study on coronene (Huo et al. 2022) we have investigated the influence of soft X-ray photon energy/final state on

the fragmentation dynamics. In the following, we apply the same approach for the four pyrene-based molecular ions under study, here. The advantage of NEXAMS as compared to conventional soft X-ray spectroscopy is the availability of separate spectra for all ionization/fragmentation channels. Fig. 6 shows a selection of these spectra for py^+ and $[\text{py} + \text{H}]^+$. The top panel shows data for NDSI into $\text{C}_{16}\text{H}_{10}^{2+}$ (a) and $\text{C}_{16}\text{H}_{11}^{2+}$ (b), respectively. In addition, spectra for single ionization accompanied by loss of s hydrogen atoms are displayed.

The NDSI data shows the same trends as observed for the much larger coronene cation (Huo et al. 2022). Most intensity is limited to the excitation regime, i.e. PIYs are very low above the 1s ionization threshold. For excitation into SOMO and LUMO, NDSI ($s = 0$) is strongest. For excitation into higher molecular orbitals, the contribution of processes with higher s increase. This is particularly clear for the broad maximum around 294 eV. Very similar trends are found for py^+ and $[\text{py} + \text{H}]^+$.

Also in the top row of panels of Fig. 6 we show the data for NDDI into $\text{C}_{16}\text{H}_{10}^{3+}$ (c) and $\text{C}_{16}\text{H}_{11}^{3+}$ (d), again accompanied by the data for loss of s H atoms. For py^+ , the 1s ionization threshold starting around 294 eV is clearly visible. As commonly found in other systems, double ionization is also observed for carbon 1s excitation. Most likely, the underlying mechanism involves two electron Auger decay (Li et al. 2021; Huo et al. 2022). For NDSI, the effect is smallest. For $[\text{py} + \text{H}]^+$, the spectra look entirely different: the ionization threshold is much less pronounced and triple cation yields are generally very low. Because this low yield is used for normalization, the resonant part of the spectrum appears very strong. It is possible that the additional hydrogen atom already weakens the molecules sufficiently to prevent efficient formation of the trications. These findings are opposite of what we had earlier observed for coronene, where single hydrogen attachment actually stabilizes the trication (Huo et al. 2022). A hydrogenation-induced weakening of the molecular structure however is in line with the findings of the Stockholm group for pyrene hydrogenation (Gatchell et al. 2015).

The NEXAMS data for most common fragments due to backbone scission are shown in the bottom row of Fig. 6 for C_7H_n^+ (e,f) and C_5H_n^+ (g,h). For both groups of fragments and for both precursor ions, there is a very smooth transition from excitation to ionization. This is quite a remarkable finding, as internal energies and initial charge of the X-ray excited/ionized system are different in both regimes. The larger C_7H_n^+ shows comparable peak intensities over the whole energy range for $n = 1, 2$. These fragments have lost most of their hydrogen content and their formation thus requires substantial excitation energy. For $n = 3$ and in particular for $n = 4$, the hydrogen to carbon ratio is similar to the 10/16 ratio of the precursor, implying that besides backbone scission, no additional hydrogen bonds needed to be broken. These fragments have highest intensity for 1s excitation to low-lying unoccupied molecular orbitals where excitation energy is small. The smaller C_5H_n^+ group of fragments exhibits a weaker dependence on n -content and the spectra generally feature higher intensities in the ionization continuum. This is a trend that is expected when going to smaller fragments because higher excitation energy and higher charge state simply favour multifragmentation into small fragments.

The next question is, how more extensive hydrogenation influences NEXAMS spectra. The data for hpy^+ and $[\text{hpy} + \text{H}]^+$ are shown in Fig. 7. A quick look back at the photofragmentation spectra of hpy^+ and $[\text{hpy} + \text{H}]^+$ in Fig. 2 reveals that the major fragments groups are similar to the $\text{py}^+ / [\text{py} + \text{H}]^+$ case, with the exception that larger dicationic fragments such as $\text{C}_{15}\text{H}_n^{2+}$ and $\text{C}_{13}\text{H}_n^{2+}$ are clearly visible. On the other hand, NDSI and NDDI as well as single and

double ionization accompanied by hydrogen loss ($[\text{C}_{16}\text{H}_{16} - s\text{H}]^{2+}$ and $[\text{C}_{16}\text{H}_{16} - s\text{H}]^{3+}$) have much lower yields as compared to the py^+ and $[\text{py} + \text{H}]^+$ cases and cannot be quantified with the accuracy required for a NEXAMS spectrum. We therefore display data for $\text{C}_{15}\text{H}_n^{2+}$ (Fig. 7a, b) and $\text{C}_{13}\text{H}_n^{2+}$ (c, d) in addition to for C_7H_n^+ (e,f) and C_5H_n^+ (g,h) which were shown in Fig. 6 as well.

The NEXAMS spectra for the large dications $\text{C}_{15}\text{H}_n^{2+}$ and $\text{C}_{13}\text{H}_n^{2+}$ are quite similar in overall structure to the data for NDDI and double ionization accompanied by multiple H loss for py^+ and $[\text{py} + \text{H}]^+$ (Fig. 6c, d). There is a clear threshold behaviour when the 1s ionization energy is reached. In the excitation regime, the normal spectral features discussed in the context of the TD-DFT calculation for hpy^+ and $[\text{hpy} + \text{H}]^+$ are observed. The relative intensities of excitation peaks with respect to the ionization continuum are higher for $\text{C}_{15}\text{H}_n^{2+}$ and $\text{C}_{13}\text{H}_n^{2+}$ from hpy^+ than for $[\text{C}_{16}\text{H}_{10} - s\text{H}]^{3+}$ from py^+ , though. For the hydrogenated $[\text{hpy} + \text{H}]^+$ precursor, the data are very similar to the $[\text{py} + \text{H}]^+$ case. The similarity of the dicationic NEXAMS data for hpy^+ and the tricationic data from py^+ is strongly indicating that double ionization of hpy^+ (and most likely also of $[\text{hpy} + \text{H}]^+$) predominantly leads to charge separation with a large dicationic fragment and a small monocationic fragment (plus possibly one or more small neutral fragments). In the process, at least six hydrogen atoms appear to be lost.

For C_7H_n^+ (Figs 7e, f) and C_5H_n^+ (Figs 7g, h), the trends are the same as observed for py^+ and $[\text{py} + \text{H}]^+$. Clearly, for the formation of these small fragments, the initial molecular structure plays only a minor role.

One of the reasons for performing the present study in the first place was to answer whether hydrogenation protects PAH cations against soft X-ray induced backbone damage. We have previously investigated this issue for coronene ($\text{C}_{24}\text{H}_{12}^+$, cor^+) and its hydrogenated counterpart ($\text{C}_{24}\text{H}_{13}^+$, $[\text{cor} + \text{H}]^+$) (Huo et al. 2022). Fig. 8 shows the relative PIYs of fragments formed from backbone fragmentation as a function of energy for both cor^+ and py^+ . For cor^+ , backbone fragmentation is at about 35 per cent the excitation regime and it increases to more than 70 per cent in the 1s ionization continuum. Hydrogenation reduces backbone fragmentation to about 30 per cent (excitation) and to about 50 per cent (ionization). For py^+ , the difference between excitation and ionization regime is much smaller than for cor^+ : backbone fragmentation increases from about 65 per cent (excitation) to about 80 per cent (ionization). Also, hydrogenation of py^+ even higher enhances backbone fragmentation systematically to 70 per cent (excitation) and 90 per cent (ionization). Also from this data, it is clear that the PAH size plays a key role not only for its photoresponse but also for the effect of hydrogen attachment. Note that for hpy^+ , backbone fragmentation is close to 100 per cent over the entire photon energy region, studied here.

4.5 Photoinduced H/H₂ loss

Besides carbon backbone fragmentation, also the soft X-ray induced loss of H and/or H₂ can be dependent on photon energy, on molecular size and on hydrogenation state.

Reitsma et al. have shown that hydrogenation can protect the structural integrity of cor^+ upon soft X-ray absorption (Reitsma et al. 2014, 2015). The underlying mechanism is loss of the extra hydrogen atoms instead of e.g. backbone fragmentation. Fig. 9 shows the $\text{C}_{16}\text{H}_n^{2+}$ (Fig. 9a, c) and $\text{C}_{16}\text{H}_n^{3+}$ (b, d) mass spectral regions for both py^+ and $[\text{py} + \text{H}]^+$ precursors (top and bottom, respectively).

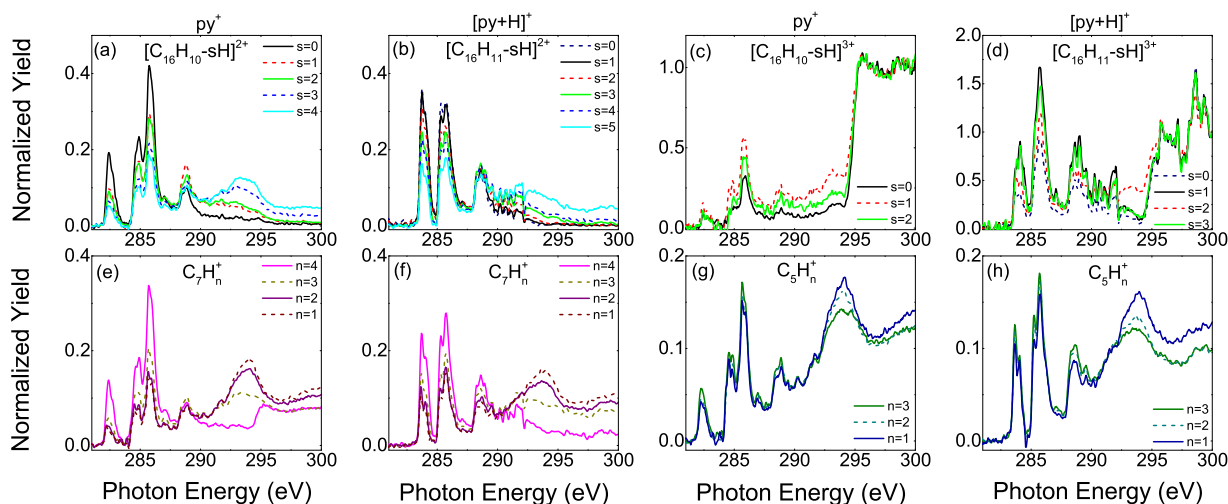


Figure 6. The top row of panels present NEXAMS data for dicationic and tricationic fragments produced from py^+ and $[\text{py} + \text{H}]^+$. Spectra for NDSI into $\text{C}_{16}\text{H}_{10}^{2+}$ (a), and into $\text{C}_{16}\text{H}_{11}^{2+}$ (b) and NDDI into $\text{C}_{16}\text{H}_{10}^{3+}$ (c), and $\text{C}_{16}\text{H}_{11}^{3+}$ (d) are shown in black. Spectra associated to loss of s H atoms are shown in colour. Dication spectra are normalized to the integral over the excitation region. Trication spectra are normalized to the average yield in the ionization region. The bottom row of panels shows data for the monocationic fragments C_7H_n^+ (e), (f) and C_5H_n^+ (g), (h).

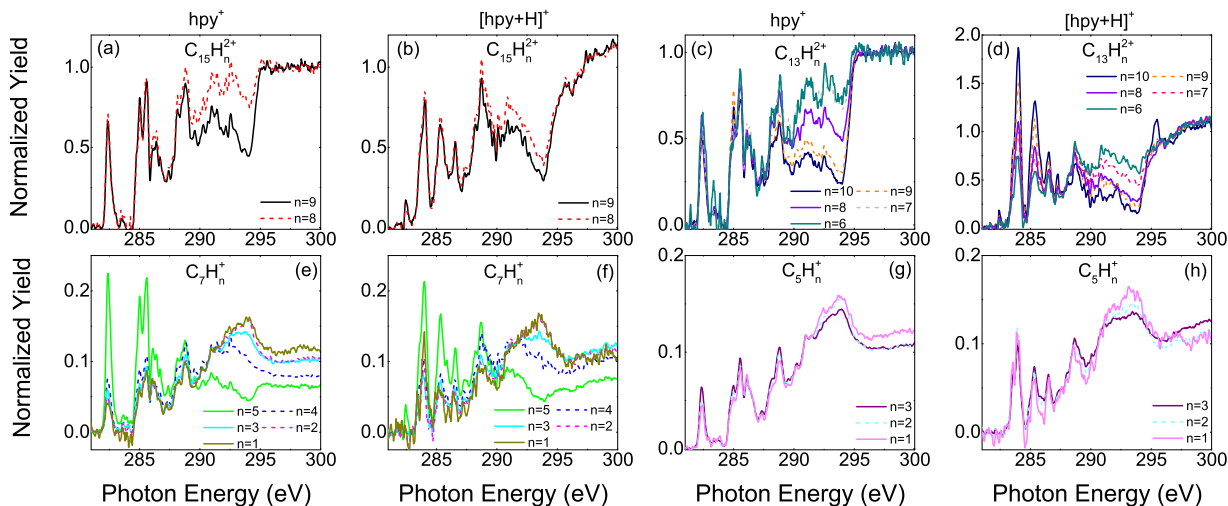


Figure 7. The NEXAMS scans of main dicationic fragments produced from hpy^+ (a, c, e, g) and $[\text{hpy} + \text{H}]^+$ (b, d, f, h). The spectra for the monocations (C_7H_n^+ and C_5H_n^+) are normalized to excitation regime. The spectra of dicationic fragments ($\text{C}_{15}\text{H}_n^{2+}$ and $\text{C}_{13}\text{H}_n^{2+}$) are normalized to the average yield in the ionization region, as were the trication spectra in Fig. 6(c, d).

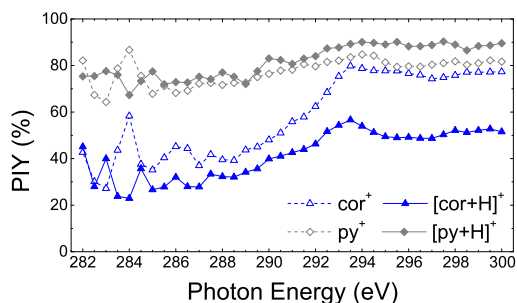


Figure 8. Relative PIY percentage of fragments due to carbon backbone fragmentation of cor^+ (blue), py^+ (grey), and their hydrogenated counterparts. The PIY percentage of cor^+ and py^+ are indicated by dashed curves while $[\text{cor} + \text{H}]^+$ and $[\text{py} + \text{H}]^+$ are displayed by solid curves.

As seen before, dicationic fragments $\text{C}_{16}\text{H}_n^{2+}$ are almost solely formed in the excitation regime, e.g. for 282.5 and 286 eV in the case of py^+ . For 1s-SOMO excitations (282.5 eV), NDSI into $\text{C}_{16}\text{H}_{10}^{2+}$ is equally intense as single ionization accompanied by H_2 loss into $\text{C}_{16}\text{H}_8^{2+}$. For 1s transitions to unoccupied π^* orbitals (286 eV), due to the slightly higher excitation energy, NDSI gets relatively weaker. Furthermore, as commonly observed in excited PAHs (Szczepanski et al. 2010; Chen et al. 2015), H_2 loss is preferred over sequential H loss, leading to even-odd oscillations in the mass spectra. At higher photon energies, direct 1s ionization occurs and NDSI is therefore quenched. Now loss of two or more H_2 moieties appears to be dominant, but those peaks are most likely due to charge separation, i.e. H_2^+ loss following a double ionization process. For $[\text{py} + \text{H}]^+$ precursors, essentially the same trends are observed, despite the fact that the precursor mass is 1 Da higher. The photoinduced loss of the

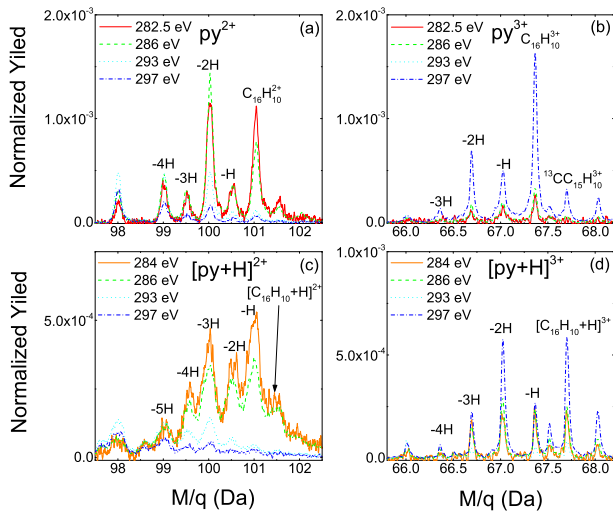


Figure 9. Mass spectra for dicationic and tricationic $C_{16}H_n$ formed after soft X-ray photofragmentation of py^+ (top row of panels) and $[py + H]^+$ (bottom row of panels).

additional H atoms leads to a shift towards higher hydrogen content, though and as a consequence the $C_{16}H_{10}^{2+}$ peak is strongest for 284 eV and for 286 eV.

Tricationic fragments $C_{16}H_n^{3+}$ show the opposite behaviour (see Fig. 9b, d). NDDI into $C_{16}H_{10}^{3+}$ (py^+) and $C_{16}H_{11}^{3+}$ ($[py + H]^+$) is observed even in the excitation regime, with very low intensity for py^+ and with intermediate intensity for $[py + H]^+$. As discussed before, 1s excitation can be followed by two-electron Auger processes and lead to double ionization. Stronger NDDI yields are observed in the ionization continuum at 297 eV. As for the dication case, H_2 loss appears to be preferred over H loss, as $[C_{16}H_{10} - 2H]^{3+}$ is stronger than $[C_{16}H_{10} - 1H]^{3+}$ (for py^+) and $[C_{16}H_{11} - 2H]^{3+}$ is stronger than $[C_{16}H_{11} - 1H]^{3+}$ (for $[py + H]^+$).

5 ASTROPHYSICAL IMPLICATIONS

5.1 Soft X-ray induced H_2 production from PAHs

In the following, we will investigate the competition between H_2 -loss and H-loss processes from py^+ and $[py + H]^+$ in neutral and ionic form. py^+ has three non-equivalent H sites and as a consequence, H-loss can lead to three different isomers. For the case of double H loss, it is assumed that both H atoms are lost from the same benzene ring, either as two consecutive atoms or as an H_2 molecule.

Fig. 10 shows the ADEs obtained by DFT for one exemplary isomeric dissociation channel. The $C_{16}H_9^{q+}$ is produced by H loss from position ‘a’ and $2H/H_2/H_2^+$ loss from neighbouring ‘a’ and ‘b’ sites results in $C_{16}H_8^{q+}$. The corresponding data for the remaining isomeric channels are provided in the supplementary material. ADEs for different isomers are almost identical. It is clear that for low charge states, neutral H_2 loss is energetically favourable. For triply charged systems, dissociation energies for H_2^+ loss and for H_2 loss become almost equal. The experimental data on the dications proves that H_2^+ loss becomes stronger with decreasing H content in the trication.

From Fig. 10(a) it can be seen that the ADE for single neutral H loss from py^+ is around 5 eV while it only is about 2.5 eV for $[py + H]^+$. In an earlier study (Holm et al. 2011), the ADE data have already been presented for H loss from py^{q+} , based on the same

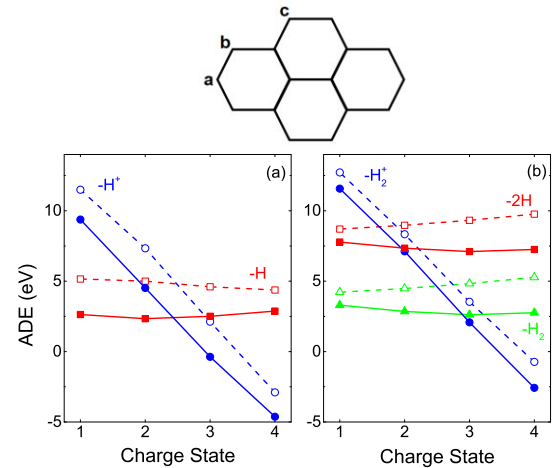


Figure 10. ADEs for fragmentation channels associated with $H/H_2/2H$ loss as a function of charge state of py^{q+} (dash curves) and $[py + H]^q+$ (solid curves). (a) H loss (squares) and H^+ loss (circles). H and H^+ are lost from the ‘a’ site (see sketch) for py^{q+} and from the ‘b’ site for $[py + H]^q+$. (b) $2H$ loss (squares), H_2^+ loss (circles), and H_2 loss (triangles) as functions of PAH charge state. $2H/H_2/H_2^+$ loss is from the ‘a’ and ‘b’ sites for both py^{q+} and $[py + H]^q+$. All calculations for $[py + H]^q+$ were all done for the h2 isomer (see Fig. 1), hydrogenated at the ‘b’ site.

functional and basis set. Herein, we further compute the ADE for similar dissociation channel for $[py + H]^q+$ to compare to py^{q+} . ADE of py^{q+} weakly decrease from 5.1 to 4.3 eV with increasing charge state. The ADE for $[py + H]^q+$ are systematically lower (by a factor of 2 for $q = 1$), but also exhibit only a weak dependency on charge state.

The ADE for H^+ loss is inversely proportional to the charge state of the three molecular cations (from positions ‘a’, ‘b’, and ‘c’) for both of py^+ and $[py + H]^+$. For $q = 1, 2$, the ADE for H^+ loss is significantly higher than the ADE for neutral H loss. For $q = 3$ the situation is reversed, and the ADE for H^+ loss becomes significantly smaller than the ADE for neutral H loss. From $q = 4$ on, py^+ precursor cations are not stable with respect to H^+ loss, anymore. $[py + H]^+$ becomes unstable with respect to H^+ loss already for $q = 3$. This clearly explains the absence of triple cation peaks in the experimental data for $[py + H]^+$.

From Fig. 10(b) it is seen that the energetics for double H/H^+ loss and for H_2/H_2^+ loss show the same trends: For $q = 1, 2$, neutral loss is energetically preferred whereas for $q = 3$, it is charge separation.

From the comparison of Figs 10(a) and (b), it is also clear that for py^+ , H_2 loss is energetically preferred, whereas for $[py + H]^+$, single H loss is preferred. In case of charge separation, H^+ loss is always energetically favourable as compared to H_2^+ loss.

It is very interesting to note, that even though ADEs for cor^+ and $[cor + H]^+$ cations (Huo et al. 2022) are very similar to the pyrene data presented in Fig. 10 both quantitatively and in q -dependence, H attachment has a stabilizing effect for cor^+ whereas it has a destabilizing effect for pyrene cations. Once again, this stresses the fact that the molecular size (and thus the vibrational temperature after X-ray absorption, Auger decay, internal conversion and internal vibrational redistribution is the key property, here.

We also note that in order to determine the prevalence of H + H loss or H_2 loss from highly excited PAHs it is very importance to account for hydrogen roaming prior to dissociation (Castellanos et al. 2018a,b). In larger astronomically relevant PAHs, the formation of the required aliphatic side groups is more likely than in small

PAHs. However, in a combined IR-spectroscopy and DFT study, it has recently been shown that H₂ loss is an important de-excitation channel for the very small py⁺ cation, as well (Panchagnula et al. 2020).

5.2 Survival of PAHs

PAH abundance and degree of ionization in XDR depend on the gas density and on the excitation energy (Maloney, Hollenbach & Tielens 1996). Siebenmorgen and Krügel have developed a model, based on unimolecular PAH photodissociation (Siebenmorgen & Krügel 2010) that allows to construct a simplified model for PAH survival in XDR. A similar model was recently further developed to predict the half-lives of PAHs in PNe (QutiáLara et al. 2018, 2020) and in regions of AGNs (Santos et al. 2022). Naturally, the results of such model calculations crucially depend on the accuracy of the employed photoabsorption cross sections.

In the following, we present a combined theoretical and experimental approach to determine soft X-ray photoabsorption cross sections for the pyrene derivatives used in this work. The photoabsorption cross section is proportional to the oscillator strength f_{lu} for a transition from the lower $|l\rangle$ state to the upper $|u\rangle$ state:

$$\sigma_{lu}(\nu) = \frac{\pi e^2}{m_e c} f_{lu} \phi_\nu \quad (1)$$

Here, c is the speed of light, e stands for the elementary charge, m_e represents the electron mass, and the ϕ_ν is a Maxwell line profile (Draine 2011).

The total photoabsorption cross section σ_{abs} must be equal to the sum of the individual cross sections σ_{lu} of all possible photoinduced processes. A photoinduced 1s vacancy in PAHs is predominantly filled by Auger decay, a process that in most cases leaves the product molecular cation strongly excited. The strong excitation will usually lead to very fast dissociation/fragmentation, such that competing slower processes such as buffer gas collisions or fluorescence can be neglected.

Experimentally, only dissociation and non-dissociative ionization (NDI) can be observed, anyway. We therefore write the photoabsorption cross section as a sum of two terms:

$$\sigma_{lu} = \sigma_{NDI} + \sigma_{dis} \quad (2)$$

Dissociation is now further divided into carbon backbone fragmentation and H loss with intact carbon backbone: $\sigma_{lu} = \sigma_{NDI} + \sigma_{C-frag} + \sigma_{H-loss}$. These partial cross sections are directly proportional to the experimentally observed PIY for the three channels (Y_{NDI} , Y_{C-frag} , and Y_{H-loss}). Thus the partial cross section for carbon backbone fragmentation can be written as:

$$\sigma_{C-frag} = \sigma_{lu} \cdot Y_{C-frag}. \quad (3)$$

We can thus express this partial cross section as a product of the total cross section (obtained from TD-DFT calculations) and the partial ion yield (obtained experimentally).

Based on the definition of the dissociation rate, we get the following equation for dissociation rate of carbon backbone:

$$k_{C-frag} = \int_{E_{min}}^{E_{max}} \sum_{l,u} \sigma_{C-frag}(E) F_{X-ray}(E) dE, \quad (4)$$

where $F_{X-ray}(E) = \frac{L_{X-ray}}{4\pi r^2 h\nu} e^{-\tau_{X-ray}}$ is the photon flux. L_{X-ray} is the X-ray luminosity. $\tau_{X-ray} = \alpha \cdot 4.6 \cdot 10^{-21} N_{H_2} \cdot \left(\frac{E}{600\text{eV}}\right)^{-2.67}$ is the X-ray optical depth where N_{H_2} stands for the column density of

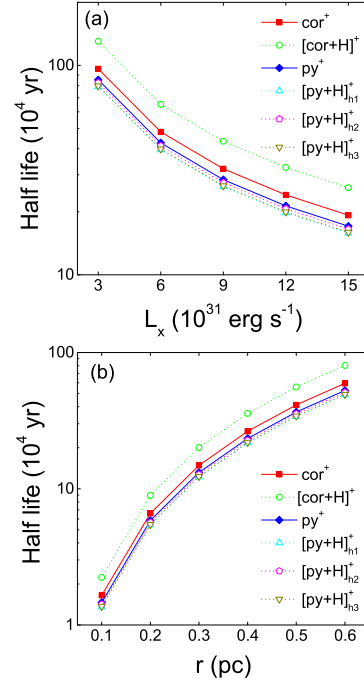


Figure 11. PAH cation half-life for cor⁺, [cor + H]⁺, py⁺, and [py + H]⁺ as a function of X-ray luminosity L_{X-ray} (a) and as a function of distance from the central star to position r (b). (a): $r=0.5$ pc; (b): $L_{X-ray} = 7 \cdot 10^{31}$ erg s⁻¹.

molecular hydrogen and the factor α depends on the photon energy ($\alpha = 0.054$ for $E < 600$ eV otherwise $\alpha = 0.11$) (Deguchi et al. 1990). In the following, we focus on the π^* transition region between $E_{min} = 282$ eV and $E_{max} = 292$ eV instead of a single photon. This more general to describe the half-life of molecular ions in evolution process. The half-life of the carbon backbone of a PAH molecular ion is then given by $t_{1/2} = \frac{\ln 2}{k_{C-frag}}$ (Andrade, Rocco & Boechat-Roberty 2010; Qutián-Lara et al. 2020).

We are now in the position to determine PAH half-life for realistic astronomical systems. NGC 7027 is an ideal young PN to study PAH survival in a carbon-rich astrophysical region of the ISM. The IR emission spectrum of NGC 7027 was obtained by the Short Wavelength Spectrometer, on board the Infrared Space Observatory (Bernard-Salas et al. 2001) and the IR telescope of the SOFIA (Lau et al. 2016). The observed IR emission bands strongly support the presence of PAHs in NGC 7027, which is also known as a bright X-ray source. In order to directly show the stability of the carbon backbone for different molecular ions, the carbon backbone half-life for cor⁺, [cor + H]⁺, py⁺, and [py + H]⁺ are presented as a function of distance (r) from NGC 7027 centre and of the X-ray luminosity (L_{X-ray}) in Fig. 11. The H₂ column density is $N_{H_2} = 1.3 \cdot 10^{21}$ cm⁻² (Agúndez et al. 2010), the luminosity is $L_{X-ray} = 7 \cdot 10^{31}$ erg · s⁻¹ (Montez & Kastner 2018), and the temperature of the X-ray emitting plasma is $T = 3.6$ MK (Montez & Kastner 2018).

Fig. 11(a), displays PAH half-life for a selection of hydrogenated and unhydrogenated PAH ions as a function of L_{X-ray} . It is clear that for all luminosities, cor⁺ has a substantially shorter half-life than [cor + H]⁺. py⁺ already has a substantially shorter half-life than cor⁺. Here, hydrogen attachment into [py + H]⁺ shortens half-life and this effect is observed for all three isomers under study. The reduction in half-life is relatively weak.

Fig. 11(b), explores the dependence of half-life from the distance to the X-ray source (QuitíáLara et al. 2020). $L_{X\text{-ray}}$ is taken as 7×10^{31} erg s⁻¹ for all positions. Again, [cor + H]⁺ has a substantially longer half-life than cor⁺ for all r , whereas py⁺ hydrogenation has an opposite, yet much weaker effect.

6 CONCLUSIONS

We have performed an experimental carbon 1s X-ray absorption spectroscopy study on cationic hydrogenated pyrene derivatives. The experimental data are in good agreement with oscillator strengths obtained by time-dependent density functional theory. From the comparison of experiment and theory, it was observed that in particular C1s- σ^* excitations strongly correlate with multiple H/H₂-losses, whereas C 1s transitions to low lying π^* orbitals favour little or no H loss.

Pyrene cations were found to be substantially more prone to soft X-ray photodissociation than coronene cations, most likely due to the higher internal temperature of photoexcited pyrene as compared to coronene. Whereas hydrogen attachment has been shown to protect coronene cations from soft X-ray photodissociation, the opposite is observed for pyrene cations, where the hydrogenated species fully dissociates after soft X-ray absorption.

In astrophysical environments, pyrene cations appear to be substantially less stable than coronene cations. Pyrene cation hydrogenation appears to have virtually no effect on the stability of carbon backbone, in contrast to the case of coronene cations, where such a protective effect is strong. It is likely that this effect limits PAH growth but favours survival of larger PAHs.

SUPPORTING INFORMATION

Supplementary data are available at *MNRAS* online.

MNRAS_2023_Soft_X_ray_of_Pyrene_Derivative_Supplementary_material_Final_Version.pdf

Please note: Oxford University Press is not responsible for the content or functionality of any supporting materials supplied by the authors. Any queries (other than missing material) should be directed to the corresponding author for the article.

ACKNOWLEDGEMENTS

We thank HZB for the allocation of synchrotron radiation beamtime. The endstation at UE52-PGM is supported by BMBF grant no. 05K16VF1. The research leading to this result has been supported by the project CALIPSOplus under the Grant Agreement no. 730872 from the EU Framework Programme for Research and Innovation HORIZON 2020. Yining Huo acknowledges funding support by the Chinese Scholarship Council (CSC). Shirin Faraji thanks the Innovational Research Incentives Scheme Vidi 2017 (project number 016.Vidi.189.044) which is financed by the Dutch Research Council (NWO). We also thank the Center for Information Technology of the University of Groningen that provides us with the Peregrine high performance computing cluster. The authors would like to acknowledge the contribution of the EU COST action MD-GAS (CA18212). The COFUND project oLife has received funding from the European Union's Horizon 2020 research and innovation programme under grant agreement no. 847675. The authors acknowledge Prof. Heloisa M. Boechat-Roberty for helpful discussions.

DATA AVAILABILITY

The data underlying this article will be shared on reasonable request to the corresponding author.

REFERENCES

- Aalto S., Muller S., Sakamoto K., Gallagher J. S., Martín S., Costagliola F., 2012, *A&A*, 546, A68
- Agúndez M., Goicoechea J. R., Cernicharo J., Faure A., Roueff E., 2010, *ApJ*, 713, 662
- Andrade D. P. P., Rocco M. L. M., Boechat-Roberty H. M., 2010, *MNRAS*, 409, 1289
- Becke A. D., 1988, *Phys. Rev. A*, 38, 3098
- Bernard-Salas J., Pottasch S. R., Beintema D. A., Wesselius P. R., 2001, *A&A*, 367, 949
- Besley N. A., Asmuruf F. A., 2010, *Phys. Chem. Chem. Phys.*, 12, 12024
- Besley N. A., Peach M. J., Tozer D. J., 2009, *Phys. Chem. Chem. Phys.*, 11, 10350
- Blik F. W., Woestenenk G. R., Hoekstra R., Morgenstern R., 1998, *Phys. Rev. A*, 57, 221
- Boschman L., Reitsma G., Cazaux S., Schlathöler T., Hoekstra R., Spaans M., González-Magaña O., 2012, *ApJ*, 761, L33
- Castellanos P., Candian A., Andrews H., Tielens A. G. G. M., 2018a, *A&A*, 616, A167
- Castellanos P., Candian A., Andrews H., Tielens A. G. G. M., 2018b, *A&A*, 616, A167
- Cazaux S. et al., 2016, *Sci. Rep.*, 6, 19835
- Cazaux S., Arribard Y., Egorov D., Palotás J., Hoekstra R., Berden G., Oomens J., Schlathöler T., 2019, *ApJ*, 875, 27
- Chen T. et al., 2015, *J. Chem. Phys.*, 142, 144305
- Costagliola F., Herrero-Illana R., Lohfink A., Pérez-Torres M., Aalto S., Muller S., Alberdi A., 2016, *A&A*, 594, A114
- Deguchi S., Izumiura H., Kaifu N., Mao X., Nguyen-Q-Rieu U. N., 1990, *ApJ*, 351, 522
- Draine B. T., 2011, *Physics of the Interstellar and Intergalactic Medium*. Princeton University Press, p. 53ff
- Epifanovsky E. et al., 2021, *J. Chem. Phys.*, 155, 084801
- Gatchell M. et al., 2015, *Phys. Rev. A*, 92, 050702
- Gavilan L., Ho P. J., Gorti U., Ogasawara H., Jäger C., Salama F., 2022, *ApJ*, 925, 86
- Hickox R. C., Alexander D. M., 2018, *Annu. Rev. Astron. Astrophys.*, 56, 625
- Hirata S., Head-Gordon M., 1999, *Chem. Phys. Lett.*, 314, 291
- Hirsch K. et al., 2009, *J. Phys. B*, 42, 154029
- Hoekstra R., Schlathöler T., de Heer F. J., Morgenstern R., 1989, *J. Phys. B*, 22, L603
- Holm A. I. S., Johansson H. A. B., Cederquist H., Zettergren H., 2011, *J. Chem. Phys.*, 134, 044301
- Huo Y. et al., 2022, *Phys. Rev. A*, 106, 063104
- Jiménez-Bailón E., Santos-Lleó M., Dahlem M., Ehle M., Mas-Hesse J. M., Guainazzi M., Heckman T. M., Weaver K. A., 2005, *A&A*, 442, 861
- Kastner J. H., Vrtilik S. D., Soker N., 2001, *ApJ*, 550, L189
- Langenberg A. et al., 2014, *Phys. Rev. B*, 90, 184420
- Lau R. M., Werner M., Sahai R., Ressler M. E., 2016, *ApJ*, 833, 115
- Lee C., Yang W., Parr R. G., 1988, *Phys. Rev. B*, 37, 785
- Lehtola S., Steigemann C., Oliveira M. J., Marques M. A., 2018, *SoftwareX*, 7, 1
- Li W. et al., 2021, *Chem. Sci.*, 12, 13177
- Maloney P. R., Hollenbach D. J., Tielens A. G. G. M., 1996, *ApJ*, 466, 561
- Montez R., Kastner J. H., 2018, *ApJ*, 861, 45
- Niemeyer M. et al., 2012, *Phys. Rev. Lett.*, 108, 057201
- Oskinova L. M., Gvaramadze V. V., Gräfener G., Langer N., Todt H., 2020, *A&A*, 644, L8
- Panchagnula S. et al., 2020, *Phys. Chem. Chem. Phys.*, 22, 21651

- Peeters E., Mackie C., Candian A., Tielens A. G. G. M., 2021, *Acc. Chem. Res.*, 54, 1921
- Postma J., Bari S., Hoekstra R., Tielens A., Schlathölder T., 2010, *ApJ*, 708, 435
- Puccetti S. et al., 2016, *A&A*, 585, A157
- Quitíán-Lara H. M., Fantuzzi F., Nascimento M. A. C., Wolff W., Boechat-Roberty H. M., 2018, *ApJ*, 854, 61
- Quitíán-Lara H. M., Fantuzzi F., Oliveira R. R., Nascimento M. A. C., Wolff W., Boechat-Roberty H. M., 2020, *MNRAS*, 499, 6066
- Rab C., Güdel M., Woitke P., Kamp I., Thi W.-F., Min M., Aresu G., Meijerink R., 2018, *A&A*, 609, A91
- Reitsma G., Boschman L., Deuzeman M. J., González-Magaña O., Hoekstra S., Cazaux S., Hoekstra R., Schlathölder T., 2014, *Phys. Rev. Lett.*, 113, 053002
- Reitsma G., Boschman L., Deuzeman M. J., Hoekstra S., Hoekstra R., Schlathölder T., 2015, *J. Chem. Phys.*, 142, 024308
- Salak D., Tomiyasu Y., Nakai N., Kuno N., Miyamoto Y., Kaneko H., 2018, *ApJ*, 856, 97
- Santos J. C., Fantuzzi F., Quitíán-Lara H. M., Martins-Franco Y., Menéndez-Delmestre K., Boechat-Roberty H., Oliveira R. R., 2022, *MNRAS*, 512, 4669
- Scott A. P., Radom L., 1996, *J. Phys. Chem.*, 100, 16502
- Siebenmorgen R., Krügel E., 2010, *A&A*, 511, A6
- Stockett M. H. et al., 2021, *ApJ*, 913, 46
- Szczepanski J., Oomens J., Steill J. D., Vala M. T., 2010, *ApJ*, 727, 12
- Tielens A., 2008, *Annu. Rev. Astron. Astrophys.*, 46, 289
- Vink J., 2012, *Astron. Astrophys. Rev.*, 20, 49
- Vosko S. H., Wilk L., Nusair M., 1980, *Canadian. J. Phys.*, 58, 1200
- Zettergren H. et al., 2021, *Eur. Phys. J. D.*, 75, 152
- Zhang Y., Kwok S., Dinh-V-Trung, 2008, *ApJ*, 678, 328
- Zhen J., Castellanos P., Paardekooper D. M., Ligterink N., Linnartz H., Nahon L., Joblin C., Tielens A. G. G. M., 2015, *ApJ*, 804, L7
- Zhen J. et al., 2016, *ApJ*, 822, 113

This paper has been typeset from a $\text{\TeX}/\text{\LaTeX}$ file prepared by the author.